Tunable active edge sites in PtSe₂ films towards hydrogen evolution reaction

Shenghuang Lin[1,†], Yang Liu[1,†], Zhixin Hu[2,†], Wei Lu[3], Chun Hin Mak[1], Longhui Zeng[1], Jiong Zhao[1], Yanyong Li[1], Feng Yan[1], Yuen Hong Tsang[1], Xuming Zhang[1], Shu Ping Lau[1,]*

[1] Department of Applied Physics, The Hong Kong Polytechnic University, Hung Hom,

Hong Kong SAR, P. R. China

[2] Lash Miller Chemical Laboratories, Department of Chemistry and Institute of

Optical Sciences, University of Toronto, 80 Saint George Street, Toronto, Ontario

M5S 3H6, Canada

[3] University Research Facility in Materials Characterization and Device Fabrication,

The Hong Kong Polytechnic University, Hung Hom, Hong Kong SAR, P. R. China

[†]These authors contributed equally to this work.

[*] Address correspondence to apsplau@polyu.edu.hk

Keywords: PtSe2, hydrogen evolution reaction, layered materials, active sites.

1

Abstract

Layered transition-metal dichalcogenides (TMDCs) have received great interest due to their potential applications in many fields including electronics, optoelectronics, electrochemical hydrogen production and so on. Recent research effort on the development of effective hydrogen evolution reaction (HER) is to modulate the active edge sites through controlling surface structure at the atomic scale. Here we firstly demonstrate a facile strategy to synthesize large-area and edge-rich platinum diselenide ($PtSe_2$) via selenization of Pt films by magnetron sputtering physical deposition method. The edge site density of the $PtSe_2$ can be effectively controlled by tuning the thickness of Pt films. The HER activity of the $PtSe_2$ can be enhanced significantly as the active edge site density increases. The maximum cathodic current density of 227 mA/cm^2 can be obtained through increasing the edge density, which well agrees with the density functional theory calculations. Our work provides a fundamental insight on the effect of active edge site density towards HER.

1. Introduction

Two-dimensional (2D) layered materials possess excellent physical, chemical and mechanical properties as compared to their 3D counterparts. They have attracted much attention around the world and revealed good potential in electronic and energy storage devices [1-12]. Transition metal dichalcogenides (TMDCs) with the chemical formula MX_2 (where M = group IVB-VIIB metal and X = chalcogen), are the members of the 2D family. TMDCs exhibit widely tunable bandgap and even remarkable semiconductor-to-metal transition. In terms of the energy storage, hydrogen possessing high energy density and zero environmental impact has been widely considered as an alternative energy carrier of the future [13, 14]. The key for achieving high efficiency of hygrogen generation is to choose high-performance hydrogen evolution reaction (HER) electrocatalysts [15]. Recently, remarkable advances have been made via utilizing TMDCs, such as MoS_2 [16-21] and WS_2 [22, 23], as electrocatalysts for HER. Among these materials, the catalytic active sites were identified theoretically [24] and experimentally to be located at the edges [25, 26]. It has also been revealed that the HER activity of MoS_2 is the dependent of the number of exposed edge sites, which have various stoichiometries, physical structures and electronic structures as compared with the (0001) basal plane of MoS_2 [25]. Based on this strategy, Kibsgaard *et al.* proposed that more active edge sites can be exposed to improve HER activity by engineering the surface structure of MoS_2 [27]. Gao *et al.* introduced a microwave-assisted method to synthesize narrow MoS_2 nanosheets with edge-terminated structure as efficient HER electrocatalyst [28]. Deng *et al.* demonstrated three-dimensional MoS_2 foam with uniform mesopores for HER activity [29]. Li *et al.* put forward a method for exposing edge sites using vertically standing MoS_2 nanosheets [30]. However, it is still challenging to control the density of edge sites.

Platinum selenide ($PtSe_2$) is a new member of TMDC family with bandgaps of 1.2 eV and 0.21 eV for monolayer and bilayer samples respectively. The multiple-layer 1T-phase $PtSe_2$ exhibits semi-metallic behaviour [31] and the $PtSe_2$ nanoparticles

show HER activity [32]. Here, we firstly demonstrate large-area and edge-rich 1T-PtSe$_2$ films prepared by selenization of magnetron sputtering deposited Pt films. The dge site density of the PtSe$_2$ films can be effectively controlled and the relationship between the edge density and the cathodic current density is established. The high HER performance of the edge-rich PtSe$_2$ films reveals a new avenue to develop edge-rich electrocatalysts.

2. Materials and Methods

2.1 Preparation of PtSe$_2$ film: Pt sputter target (99.99% purity) was purchased from Kurt J Lesker. Pt films with different thicknesses were firstly deposited on fluorine-doped tin oxide (FTO) and SiO$_2$/Si substrates using a sputtering system. Then the Pt samples were loaded into a tube furnace and placed at the center of the quartz tube and heated to 400 °C. The Se source was palecd away from the Pt films with a distance of 10-15 cm. Argon gas with a flow rate of 40 sccm, was used to transport the vaporized Se to the Pt films. Prior to the heating process, argon gas with a flow rate of 300 sccm was purged the system for 20 min. Then a dwell time of 1 hours was used to ensure complete selenization. A transfer method was adopted to deposit PtSe$_2$ film onto the glassy carbon electrode. Firstly, the PtSe$_2$ film was prepared onto SiO$_2$/Si substrate using the two steps method as described above. Then a protective layer of polymethyl methacrylate (PMMA) was spin coated onto the PtSe$_2$ film. After that, the substrate with the PMMA coated PtSe$_2$ was placed into a NaOH bath. The detached PMMA coated PtSe$_2$ film was then transferred to the glassy carbon electrode. Acetone was used to remove the PMMA.

2.2 Physical Characterizations of PtSe$_2$: Raman spectra were collected using a Horiba Jobin Yvon HR800 Raman microscopic system equipped with a 488 nm laser operating at 180 mW. The spot size of the excitation laser is ~1 μm. The AFM measurements were performed in a Veeco Dimension-Icon system with a scanning rate of 0.972 Hz. The microstructure of the PtSe$_2$ was observed by a JEM-2100F scanning transmission electron microscope (STEM) equipped with energy dispersive X-ray (EDX) operated at 200 kV. X-ray diffraction (XRD) was carried out with a

Rigaku SmartLab X-ray diffractometer (Cu KR radiation λ=1.54 Å) operating at 45 kV and 200 mA. XPS (KRATOS Analytical, AXIS Ultra DLD) was carried out to analyze the chemical composition of the samples.

2.3 Electrochemical characterization of PtSe$_2$: The electrochemical measurements were carried out in a three-electrode system using a CHI 660E potentiostat. The PtSe$_2$ films with different thicknesses (1.9 nm to 76 nm) were transferred onto glassy carbon (GC) disk electrodes which served as the working electrodes with a platinum (Pt) counter electrode and an Ag/AgCl (saturated KCl) reference electrode (Hach). All linear scanning voltammetry (LSV), Tafel plots and A.C. impedance (EIS) of the samples were conducted using a 0.5M sulfuric acid (H$_2$SO$_4$) electrolyte prepared in Millipore water (18 MΩ cm). All potentials reported in this work were given with respect to the reversible hydrogen electrode (RHE), which were calibrated by the following equation: Evs RHE = Evs Ag/AgCl + 0.059 × pH + 0.199 (V) [39]. Bare GC and Pt electrodes were also performed with the same measurement for comparison.

2.4 DFT calculations: The adsorption structure of H atom on bare and defected surface was simulated with a 4×4 supercell of 2L-PtSe$_2$. The slab was separated by a 30 Å vacuum space. The 1T-edge was simulated using a 2×3×2 slab model, with x direction being continuous while y and z directions separated by vacuum slabs. A 3×3×1 k-mesh was used to sample the first Brillouin zone of unit cell on 2L-PtSe$_2$. The 1T-edge unit cell was sampled by a k-mesh with similar density. All atoms were relaxed until the residual force for each atom is less than 0.01 eV·Å^{-1}. Size of the supercell is reduced when calculating vibrational frequencies. Details can be found in the supporting information.

3. Results and discussion

Firstly, Pt films with different thicknesses were deposited on SiO$_2$/Si substrates using a sputtering system. Then the controllable edge-rich PtSe$_2$ films with different thicknesses could be synthesized on substrates by direct selenization of Pt films at a temperature of 420 °C. The growth procedure is illustrated in **Figure 1a** and **b.** The

details are described in **Materials and Methods**. **Figure 1c** shows the photos of the as-prepared $PtSe_2$ films with thicknesses ranging from 1.9 nm to 76 nm on SiO_2/Si substrates. The crystal structure of $PtSe_2$ consists one layer of Pt atoms sandwiched between two layers of Se atoms. **Figure 1d** shows the Raman spectrum of the $PtSe_2$ (11.4 nm thick) revealing two feature peaks located at 189.4 cm^{-1} and 220.3 cm^{-1}, which correspond to E_g in-plane and A_{1g} out-of-plane Raman active modes respectively [33]. The additional peak located at 231 cm^{-1} is corresponding to a LO (longitudinal optical) mode involving the out-of-plane and in-plane motions of Pt and Se atoms. It should be noted here that the E_g mode represents the in-plane vibration of Se atoms but the A_{1g} mode describes the out-of-plane vibration of Se atoms. The Raman spectra of the $PtSe_2$ films with different thicknesses are shown in **Figure S1a**. The E_g mode of the $PtSe_2$ is red-shifted by around 5 cm^{-1} when the thickness increases from 1.9 nm to 76 nm, similar to that observed in the E^1_{2g} mode in MoS_2 [33], while the A_{1g} mode shows nearly no shift. Interestingly, the Raman intensity of the A_{1g} mode shows a significant increase when increasing the thickness of the $PtSe_2$ films, which might be induced by the enhancement of out-of-plane interactions through the increase of layer numbers [33]. The $PtSe_2$ film with a thickness of 7.6 nm (its correspongding atomic force microscope (AFM) profile is shown in **Figure S1c,** the AFM images of other samples can be found in **Figure S2**) was annealed for 30, 60, 90 and 120 min. The Raman spectra of the $PtSe_2$ films as a function of annealing time is shown in **Figure S1b**. No obvious shift can be observed in their Raman peaks. In addition, the $PtSe_2$ film annealed for 90 min possesses a highest Raman intensity among the studied samples. The Raman intensity decreases as the annealing time increases further. It may be attributed to the creation of defects or Se vancancies which degrade the crysal quality and in turn reduce the Raman intensity. Thus, the annealing time of 90 min was chosen to prepare all the samples. To further confirm the crystal structure of the as-prepared $PtSe_2$ films, X-ray diffraction (XRD) was performed. **Figure S1d** shows the XRD pattern of the $PtSe_2$ sample (38 nm). The $PtSe_2$ film possesses two pronounced peaks located at 16.5° and 44.3° corresponding to the (0 0 1) and (1 1 1) crystal planes respectively.

Besides SiO_2/Si substrate, the $PtSe_2$ films can also be grown onto FTO glass substrates as shown in **Figure S1e**. The inset reveals a typical Raman spectrum of the $PtSe_2$ film on FTO. The Raman spectra of the $PtSe_2$ films with different thicknesses (ranging from 3.8 nm to 76 nm) on FTO can be found in **Figure S1f**. **Figure S1g** shows the X-ray photoelectron spectroscopy (XPS) result, which clearly depicts the Pt-related peaks (*i.e.*, Pt-$4f_{5/2}$ at 72.9 eV and Pt-$4f_{7/2}$ at 76.2 eV) and the Se-related peaks (*i.e.*, Se-$3d_{3/2}$ at 54.3 eV and Se-$3d_{5/2}$ at 55.1 eV), corresponding to the reported values for $PtSe_2$ film [32]. The oxidation states of Pt and Se can be found in Figure S1h and S1i, respectively. For the Pt 4f spectrum, a primary peak located at ~72.9 eV is attributed to $PtSe_2$. The peaks loacted at ~71.5 eV, ~74.6 eV and ~75.2 eV are corresponded to unreached Pt metal whereas the one located at ~77.4 eV is attributed to oxides (i.e. PtO_x). By comparing the relative atomic percentages of $PtSe_2$, Pt (5.5 at.%) and PtO_x (1.8 at.%), we can conclude that the majority of the Pt has been transformed into $PtSe_2$ (92.7 at.%). As for the Se 3d spectrum, besides the primary peak from PtSe, the other peaks located at 52.8 eV and 58 eV are attributed to Se and Se-O respectively. **Figure S1j** depicts the UV–vis–NIR absorption spectra of the $PtSe_2$ films with different thicknesses on FTO. There is one pronounced UV absorption peak located at 398 nm for the 1.9 nm thick $PtSe_2$ film, which is red-shifted by 16 nm to 414 nm as the thickness increased to 76 nm. As the thickness increases, the three peaks located at 451 nm, 492 nm and 542 nm become more prominent. Meanwhile, the absorption intensity of the $PtSe_2$ increases with the increasing thickness, which is confirmed by the colour changes of the $PtSe_2$ on FTO as shown in **Figure S1e**. Moreover, the absorption spectra are broad covering from UV to NIR regions, revealing its potential in optoelectronic applications.

In order to investigate the microstructural properties of the $PtSe_2$ films, the scanning transmission electron microscopy (STEM) characterization was performed. **Figure S3a-c** represent low-magnification top-view TEM images of the $PtSe_2$ film with a thickness of 3.8 nm. It can be seen that the obtained film is nearly continuous. The inset in **Figure S3c** shows the selected area electron diffraction (SAED) pattern, which confirms the obtained sample is polycrystalline and the five distinguished dash

red circles are assigned to (100), (110), (200), (113) and (122) planes with lattice spacings of 3.25, 1.82, 1.64, 1.24 and 1.11 Å respectively. **Figure S3d** reveals the corresponding high-resolution transmission electron microscopy (HRTEM) image. The crystal plane spacing of the sample is ~0.182 nm, which corresponds to (110) crystal plane of the $PtSe_2$. Here we can find the main surface sites on the basal planes are terrace sites, which is similar to that in MoS_2 [34]. Interestingly, the main surface sites are turned into edge sites when the film thickness increases. **Figure 2a** shows the low-magnification TEM images of the $PtSe_2$ film (38 nm thick). The vertically aligned layers standing on the surface are shown in **Figure 2b-e**. The inset in **Figure 2b** reveals seven distinguished dash red circles assigned to (001) (100), (011), (012), (110), (111) and (201) planes with lattice spacing of 5.21, 3.25, 2.74, 2.01, 1.83, 1.77 and 1.54 Å respectively, which reveals its polycrystalline structure. The HRTEM image as shown in **Figure 2e** clearly reveals the periodic atom arrangement of the $PtSe_2$ film at a selected location, which exhibits the same lattice spacing of 0.52 nm in different vertical domains as marked by the yellow arrows. The inset reveals the linescan profile as indicated by the red dashed arrow, which shows that the layer-to-layer spacing is 5.2 Å, corresponding to (0 0 1) crystal plane. The STEM EDS (energy-dispersive X-ray spectroscopy) result is shown in **Figure 2f**. It confirms that the studied sample consists of Pt and Se elements. The STEM-EDS mapping images (**Figure S4**) also clearly show the presence of Pt and Se elements, and a perfect match between the Pt and Se elements are visible.

In order to estimate the edge density of the $PtSe_2$ thin films as a function of the film thickness, we have developed a method by applying image analysis tool to reveal the edge structures of the sample in a TEM image. **Figure S5a** shows the TEM image of a 57 nm thick $PtSe_2$ film. The fast Fourier transform (FFT) of the image is shown in **Figure S5b**. The edge structures can be separated by filtering the reciprocal space (i.e. FFT of the original image) using selective masks on the reflexes corresponding to the interlayer spacing of $PtSe_2$. After reconstructions by inverse FFT (**Figure S5c**), the contrast of the edge structures can be enhanced while the domains in other crystal directions are suppressed. Then the Gaussian blurring is applied (**Figure S5d**) to

reduce the lattice contrast and appropriate threshold for the edges of the vertically grown domains are digitalized based on direct correlation with the original TEM image (**Figure S5e**). The total area coverage of the vertically grown domains can be retrieved (**Figure S5f**) by the Analyze Particles function in the ImageJ software. The edge coverage density is estimated to be ~48%. By applying the above image anlaysis technique, the edge denisty of the PtSe$_2$ thin films based on at least three regions with various thicknesses are listed in Table 1. As the thickness of the PtSe$_2$ film increases from 3.8 nm to 76 nm, the edge density increases from ~0 to ~81%, which could be confirmed by observing the increase of edge sites on the surface of PtSe$_2$ by increasing its thickness as shown in **Figure S6**. It should be noted that the edge density here only represents the coverage of the edge structures on the top surface. The edge structures can also be found below the top surface.

The morphologies and the growth process of our edge-rich PtSe$_2$ films are similar to the MoS$_2$ and MoSe$_2$ with vertically aligned layers [34]. The growth mechanism of our edge-rich PtSe$_2$ films may also follow the one proposed by the authors where the chemical conversion occurs much faster than the diffusion of the Se gas into the film. Thus the diffusion along the layers through van der Waals gaps is expected to be much faster across the layers. Accordingly, the layers naturally orient perpendicular to the film. The thicker the Pt films provide a larger density of edge structures.

It has been reported that the edge-terminated MoS$_2$ films exhibited excellent HER performance [34] and even could achieve highly efficient water disinfection property [35]. Thus, it then prompts us to investigate the HER performance of the edge-rich PtSe$_2$ films theoretically and experimentally. The activity of HER is highly related to the variance of free energy during the reaction process. An ideal catalyst should have moderate interaction with the reagent according to the Sabatier's principle [36], i.e., the free energy of adsorption structure is close to that of reagent and product. **Figure 3a** shows the change of free energy during the H$_2$ generation reaction on different adsorption sites. Four types of sites are considered in the comparison, including bare surface, antisite defect with a Se atom replaced by Pt (Pt$_{se}$ antisite), Se-vacancy, and 1T-edge. These sites were selected since antisite and vacancy defects are common in

TMDs [37] and 1T-edge is the most stable edge of PtSe$_2$ [38]. 2L slab models of PtSe$_2$ in 1T-phase were used for calculating the free energy of H-atom adsorption on bare surface and point defects. Increasing the thickness will make the electronic structure more consistent with the experiment. But the adsorption energy or vibration frequencies of H atom are not sensitive to the thickness. The Slab model and adsorption structures are shown in **Figure S7**. In the free-energy diagram, reagent and product are considered to have the same free energy, indicating an equilibrium state. The free energy of adsorbed H atom is highly related to the site. H atom on 1T-edge site has the free energy (-0.02 eV) closest to that of gas-phase H$_2$ or H$^+$ ion, consistent to the previous study [31]. The second candidate for HER is Se-vacancy site, which gives a free energy difference of 0.13 eV. In both cases the H atom directly bonds to an unsaturated Pt atom, showing the top site of the unsaturated Pt atom is the better site to adsorb H atom. The conclusion is different from that on MoS$_2$, in which the unsaturated S atom is more active [39]. Se-vacancy on the surface contributes to the reaction if there are plenty of them on the surface. In addition, the existence of vacancy gives a wider range of light absorption [37], which also promotes the reaction. On the other hand, the bare surface and Pt$_{Se}$ antisite are less active in HER as the H-substrate interaction is weaker. Therefore, it is necessary to create enough 1T-edge site or se-vacancy on PtSe$_2$ surface to enhance the HER activity.

Other than its negative free energy, the advantage of 1T-PtSe$_2$ as the HER electrocatalyst is also manifested by investigating its electronic structures. **Figure 3b** shows the partial density of states (PDOS) plots for the above considered adsorption sites. The bilayer PtSe$_2$ without defects has a bandgap of only 0.3 eV. It worth mentioning that the sample used in the experiment should be metallic due to their multilayer nature and strong interlayer hybridization [40]. PDOS of PtSe$_2$ with V$_{Se}$ and Pt$_{Se}$ have similar appearance as compared with the bare surface, indicating that low-coverage (1/16 ML) defects do not drastically affect the conductivity of the substrate. The 1T-edge model has larger density of states around Fermi-level. It indicates that the PtSe$_2$ is more metallic if 1T-edge exists. Thus, the simulation results

reveal that IT-phase PtSe$_2$ with high density of edges could be an efficient HER catalyst.

In order to investigate the electrocatalytic HER activity of the PtSe$_2$ films, linear scanning voltammetry (LSV) was carried out in a standard three-electrode configuration in 0.5 M H$_2$SO$_4$ solution. The as-prepared PtSe$_2$ films was attached onto a glassy carbon (GC) disk electrode to serve as working electrode. Ag/AgCl and platinum (Pt) were selected as the reference and counter electrode, respectively. Bare GC and Pt electrodes were also characterized under the same measurement conditions for comparison.

Figure 4a depicts the schematic illustration of the H$_2$ generation on the edge-rich PtSe$_2$ films. **Figure 4b** shows the polarization curves of the PtSe$_2$ films with different thicknesses (from 1.9 nm to 76 nm). Towards the negative potential direction, cathodic current rises rapidly due to the electrocatalytic reduction of protons to H$_2$. It can be seen that all the PtSe$_2$ electrodes exhibit electrocatalytic HER activity. Interestingly, the cathodic current density increases as the thickness of the PtSe$_2$ films increases. The maximum current density of 227 mA/cm^2 is achieved on the PtSe$_2$ film with a thickness of 76 nm, which is much better than that of the GC electrode and about half of the current density of the Pt electrode. In addition, the smallest onset overpotential recorded on the PtSe$_2$ electrode is located at -170 mV vs. RHE, corresponding to a small HER overpotential of ~327 mV at a current density of 10 mA/cm^2. In sharp contrast, the bare GC electrode is poor with an onset overpotential about 787 mV. This result suggests that the PtSe$_2$ electrode promotes proton reduction process. This phenomenon can be attributed to the high edge density on the surface of the PtSe$_2$ films. As shown in **Figure 4c**, a linear relationship between the edge denisty and the current density is established. As the edge denisty increases, the current density is also increases which is in good agreement with the simulation results. Therefore, the edge-rich PtSe$_2$ films play a key role in enhancing the HER activity.

Moreover, Tafel slope is an another common and useful indicator to evaluate the performance of the HER catalyst. The corresponding values of the samples can be

calculated according to the Tafel equation ($\eta = b \log(j) + a$) [41], where η, b and j represent the overpotential, Tafel slope and current density respectively; a is a constant. Accordingly, the Tafel slopes for the $PtSe_2$ with different thicknesses can be found in **Figure 4d**, which reveals the values of Tafel slope ranging from 32 to 63 mV/decade. It is worth noting that, the smallest Tafel slope of ~32 mV/decade for $PtSe_2$ is comparable to that of the Pt/C catalyst or even smaller than that of many other 2D HER catalysts [42-45], indicating the exceptional activity of $PtSe_2$ towards H_2 evolution reaction. Meanwhile, the exchange current density, j_0, can be determined by fitting the linear portion of Tafel plot at low cathodic current based on the Tafel equation [34], yielding a value of 1.5×10^{-5} A/cm^2 for 76 nm $PtSe_2$. Then a turn over frequency (TOF) at 0 V of 0.054 s^{-1} for $PtSe_2$ can be obtained (Table 2), which is 4 times that of MoS_2 and $MoSe_2$, revealing the better catalyst efficiency of $PtSe_2$.

In addition, high activity and good stability are equally important for an advanced HER catalyst. Therefore, the current-time curve of the $PtSe_2$ electrode was examined in 0.5 M H_2SO_4 solution. As shown in **Figure 4e** and **Figure S8**, the overpotential of the $PtSe_2$ electrode with current density of 10 mA/cm^2 current density increases by only 4 mV after 1000 potential cycles. **Figure 4f** is the photo of the $PtSe_2$-coated GC electrode covered by many bubbles, implying the effective HER activity of edge-rich $PtSe_2$ film.

4. Conclusion

In summary, we demonstrate a facile way to prepare scalable and edge-density controllable $PtSe_2$ films by direct selenization of Pt films magnetron sputtering physical deposition method. The edge density of the $PtSe_2$ films can be as high as 81% with a maximum cathodic current density of 227 mA/cm^2. A linear relationship between edge density and the HER activity is established which is in good agreement with the simulation results. Our work opens a new pathway for preparing edge-density controllable materials for HER system.

Acknowledgements

Reference

1. K. Mak, C. Lee, J. Hone, J. Shan, T. F. Heinz. *Phys. Rev. Lett.* 105 (2010) 136805.

2. A. Splendiani, L. Sun, Y. Zhang, T. Li, J. Kim, C. Chim, G. Galli, F. Wang. *Nano Lett.* 10 (2010) 1271-1275.

3. B. Radisavljevic, A. Radenovic, J. Brivio, V. Giacometti, A. Kis. *Nat. Nanotechnol.* 6 (2011) 147-50.

4. J. Feng X. Qian C. Huang, J. Li. *Nat. Photonics* 6 (2012) 866-872.

5. M. Bernardi, M. Palummo, J. C. Grossman. *Nano Lett.* 13 (2013) 3664-3670.

6. O. Lopez-Sanchez, D. Lembke, M. Kayci, A. Radenovic, A. Kis. *Nat. Nanotechnol.* 8 (2013) 497.

7. G. L. Frey, K. J. Reynolds, R. H. Friend, H. Cohen, Y. Feldman. *J. Am. Chem. Soc.* 125 (2003) 5998.

8. S. Lin, S. Liu, Z. Yang, Y. Li, T.W. Ng, Z. Xu, Q. Bao, J. Hao, C.-S. Lee, C. Surya, F. Yan, S.P. Lau, *Adv. Func. Mater.* 26 (2016) 864-871.

9. Y. Yoon, K. Ganapathi, S. Salahuddin. *Nano Lett.* 11 (2011) 3768-3773

10. A. K. Geim. *Science* 324 (2009) 1530–1534.

11. F. Schwierz. *Nat. Nanotechnol.* 5 (2010) 487-96.

12. S. Lin, Y. Li, W. Lu, Y.S. Chui, L. Rogée, Q. Bao, S.P. Lau. *2D Mater.* 4 (2017) 025001.

13. M. S. Dresselhaus, I. L. Thomas. *Nature* 414 (2001) 332–337.

14. J. A. Turner. *Science* 305 (2004) 972–974.

15. M. G. Walter, E. L. Warren, J. R. McKone, S. W. Boettcher, Q. Mi, E. A. Santori, N. S. Lewis, Solar Water Splitting Cells. *Chem. Rev.* 110 (2010) 6446–

6473.

16. A. B. Laursen, S. Kegnaes, S. Dahl, I. Chorkendorff. *Energy Environ. Sci.* 5 (2012) 5577–5591.

17. C. G. Morales-Guio, X. L. Hu. *Acc. Chem. Res.* 47 (2014) 2671–2681.

18. D. Merki, X. L. Hu. *Energy Environ. Sci*. 4 (2011) 3878–3888.

19. L. Liao, S. Wang, J. Xiao, X. Bian, Y. Zhang, M. D. Scanlon, X. Hu, Y. Tang, B. Liu, H. H. Girault. *Energy Environ. Sci*. 7 (2014) 387–392.

20. Z. Lu, W. Zhu, X. Yu, H. Zhang, Y. Li, X. Sun, X. Wang, H. Wang, J. Wang, J. Luo, X. Lei, L. Jiang. *Adv. Mater*. 26 (2014) 2683–2687.

21. Z. Chen, D. Cummins, B. N. Reinecke, E. Clark, M. K. Sunkara, T. F. Jaramillo. *Nano Lett*. 11 (2011) 4168–4175.

22. D. Voiry, H. Yamaguchi, J. Li, R. Silva, D. C. B. Alves, T. Fujita, M. Chen, T. Asefa, V. B. Shenoy, G. Eda, M. Chhowalla. *Nat. Mater.* 12 (2013) 850–855.

23. L. Cheng, W. Huang, Q. Gong, C. Liu, Z. Liu, Y. Li, H. Dai. *Angew. Chem. Int. Ed*. 53 (2014) 7860–7863.

24. B. Hinnemann, P. G. Moses, J. Bonde, K. P. Jørgensen, J. H. Nielsen, S. Horch, I. Chorkendorff, J. K. Nørskov. *J. Am. Chem. Soc*. 127 (2005) 5308–5309.

25. T. F. Jaramillo, K. P. Jørgensen, J. Bonde, J. H. Nielsen, S. Horch, I. Chorkendorff. *Science* 317 (2007) 100–102.

26. H. I. Karunadasa, E. Montalvo, Y. Sun, M. Majda, J. R. Long, C. J. Chang. *Science* 335 (2012) 698–702.

27. J. Kibsgaard, Z. Chen, B. N. Reinecke, T. F. Jaramillo. *Nat. Mater.* 11 (2012) 963-969.

28. M. Gao, M. K.Y. Chan, Y. Sun. *Nature Commun.* 6 (2015) 7493.

29. J. Deng, H. Li, S. Wang, D. Ding, M. Chen, C. Liu, Z. Tian, K. S. Novoselov, C. Ma, D. Deng, X. Bao. *Nature Commun.* 8 (2017) 14430.

30. H. Li, H. Wu, S. Yuan, H. Qian. *Scientific Reports* 6 (2015) 21171.

31. Y. Wang, L. Li, W. Yao, S. Song, J. T. Sun, J. Pan, X. Ren, C. Li, E. Okunishi, Y. Wang, E. Wang, Y. Shao, Y. Y. Zhang, H. Yang, E. F. Schwier, H. Iwasawa, K. Shimada, M. Taniguchi, Z. Cheng, S. Zhou, S. Du, S. J. Pennycook, S. T.

Pantelides, H. Gao. *Nano Lett*. 15 (2015) 4013.

32. X. Chia, A. Adriano, P. Lazar, Z. Sofer, J. Luxa, M. Pumera. *Adv. Funct. Mater*. 26 (2016) 4306–4318.

33. C. Yim, K. Lee, N. McEvoy, M. O′Brien, S. Riazimehr, N. C. Berner, C. P. Cullen, J. Kotakoski, J. C. Meyer, M. C. Lemme, G. S. Duesberg. *ACS Nano* 10 (2016) 9550–9558.

34. D. Kong, H. Wang, J. J. Cha, M. Pasta, K. J. Koski, J. Yao, Y. Cui. *Nano Lett.* 13 (2013) 1341−1347.

35. C. Liu, D. Kong, P. Hsu, H. Yuan, H. Lee, Y. Liu, H. Wang, S. Wang, K. Yan, D. Lin, P. A. Maraccini, K. M. Parker, A. B. Boehm, Y. Cui. *Nature Nanotechnology* 11 (2016) 1098–1104.

36. J. Cheng, P. Hu. *J. Am. Chem. Soc.* 130 (2008) 10868–10869.

37. J. Hong, Z. Hu, M. Probert, K. Li, D. Lv, X. Yang, L. Gu, N. Mao, Q. Feng, L. Xie, J. Zhang, D. Wu, Z. Zhang, C. Jin, W. Ji, X. Zhang, J. Yuan, Z. Zhang. *Nat. Commun*. 6 (2015) 6293.

38. C. Tsai, K. Chan, J. K. Nørskov, F. Abild-Pedersen. *Surf. Sci.* 640 (2015) 133–140.

39. D. Voiry, J. Yang, M. Chhowalla. *Adv. Mater.* 28 (2016) 6197–6206.

40. Y. Zhao, J. Qiao, Z. Yu, P. Yu, K. Xu, S. Lau, W. Zhou, Z. Liu, X. Wang, W. Ji, Y. Chai. Adv. Mater. 29 (2016) 1604230.

41. M. Zeng, Y. Li. *J. Mater. Chem. A* 3 (2015) 14942–14962.

42. Y. Shi, B. Zhang. *Chem. Soc. Rev.* 45 (2016) 1529- 1549**.**

43. Q. Lu, Y. Yu, Q. Ma, B. Chen, H. Zhang. *Adv. Mater.* 28 (2016) 1917–1933.

44. Z. Wu, J. Wang, R. Liu, K. Xia, C. Xuan, J. Guo, W. Lei, D. Wang. *Nano Energy*, 32 (2017) 511–519.

45. C. Bae, T. A. Ho, H. Kim, S. Lee, S. Lim, M. Kim, H. Yoo, J. M. Montero-Moreno, J. H. Park. H. Shin. *Sci. Adv.* 3 (2017) e1602215.
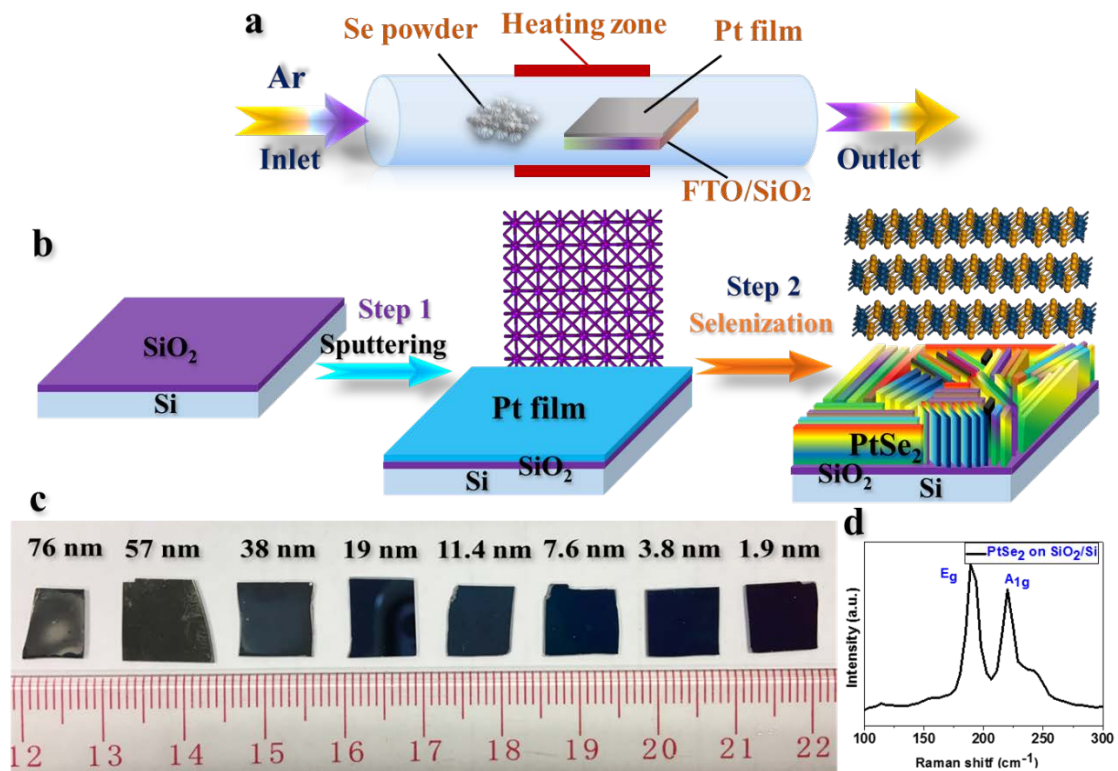
Figure 1. (a) Schematic illustrations of the growth process for PtSe$_2$. (b) Two-step growth method for the synthesis of PtSe$_2$ film. Step 1: deposition of Pt film on SiO$_2$/Si substrate by magnetron sputtering. Step 2: Selenization of the Pt film into PtSe$_2$. (c) Photo of the as-prepared PtSe$_2$ films with various thicknesses. (d) A typical Raman spectrum of the PtSe$_2$ film on SiO$_2$/Si.
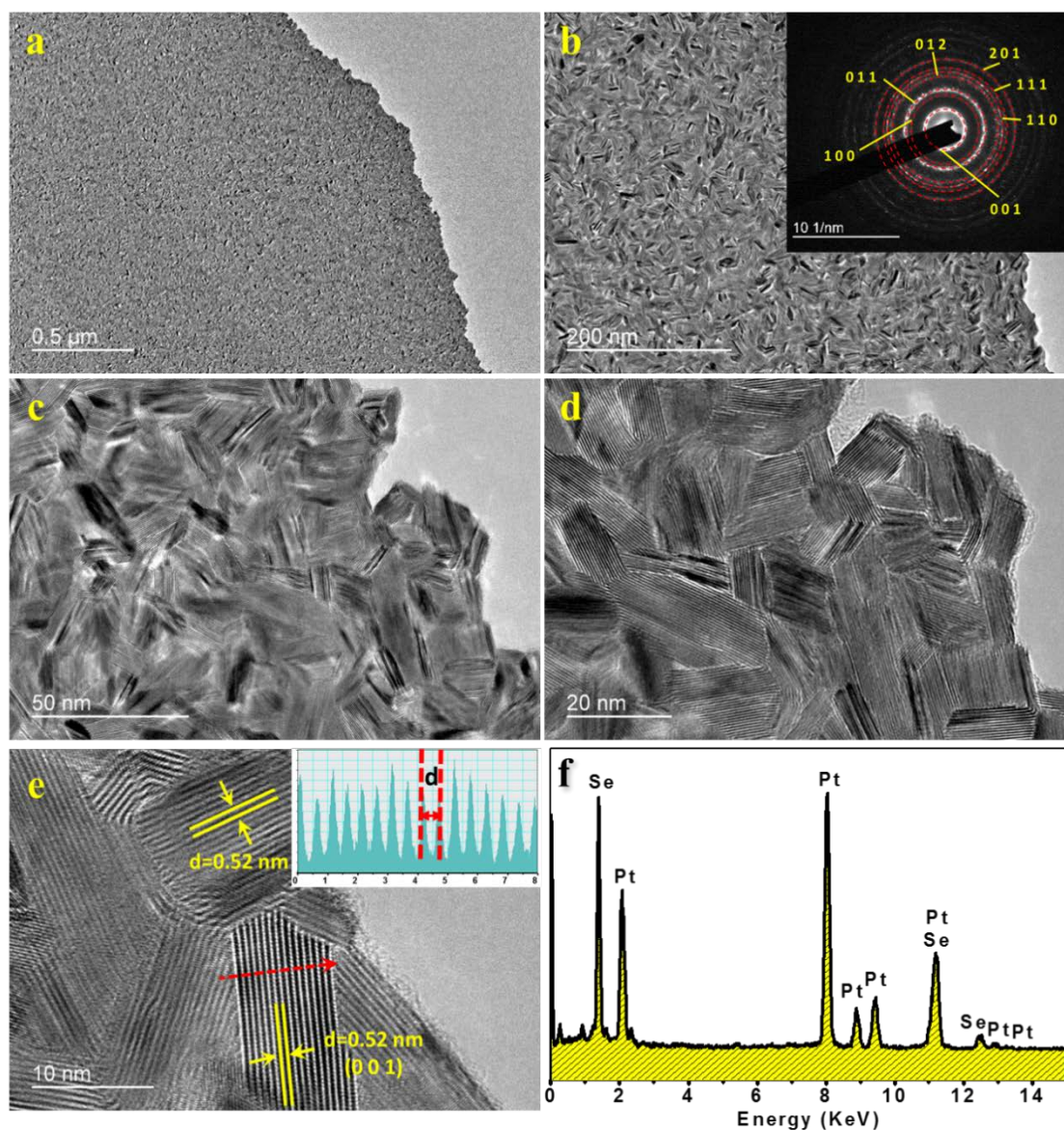
Figure 2. (a) TEM image of a 38 nm thick PtSe$_2$ film. (b)-(e) Local zoom-in of the areas corresponding to (a); the inset in (b) shows the SAED result of the sample; the TEM image (e) where the Se–Pt–Se layers are resolved, the inset in (e) reveals the layer-to-layer spacing is 5.2 Å. (f) EDX result of the studied sample.
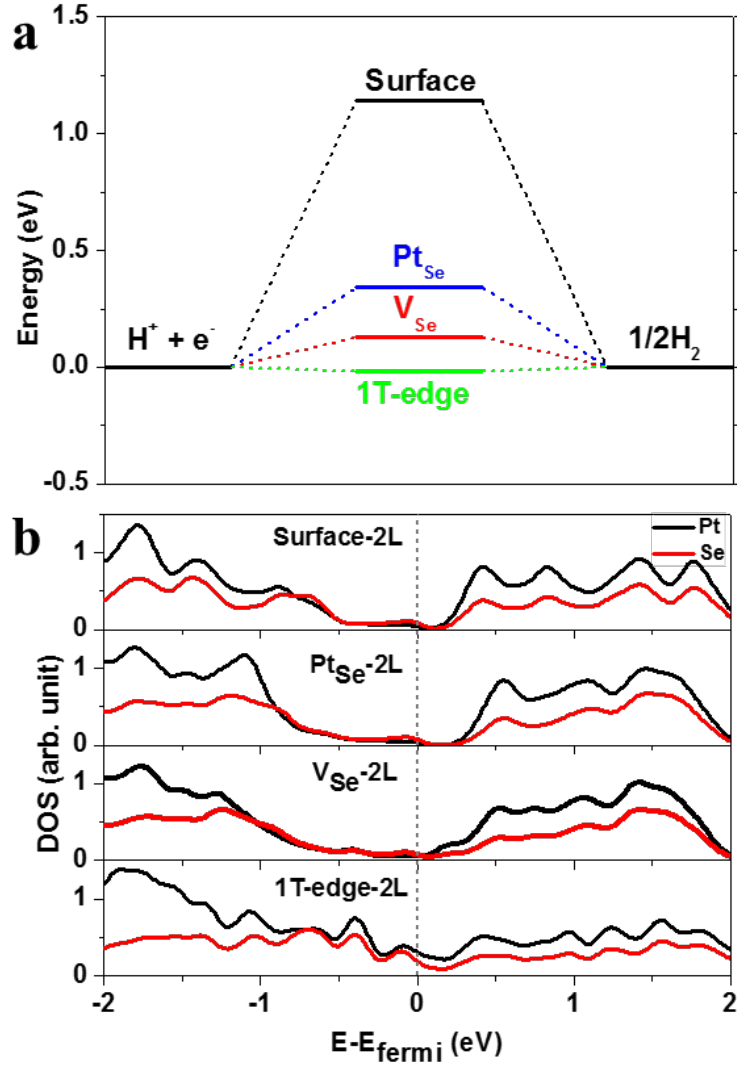
Figure 3. Simulated free-energy diagram and partial density of states (PDOS). (a) free-energy diagram for HER on bare surface, antisite defect with an Se replaced by Pt (Pt_{Se}), Se-vacancy (V_{Se}) and 1T-edge at low coverage ($\leq 1/4$ ML). The value is for standard condition with 1 bar of H_2, PH = 0, and T = 300K. Ionic H and gas phase H_2 have the same free energy to model an equilibrium state, which is also used as the zero energy-level. (b) PDOS for Pt (black) and Se (red) in considered adsorption structures. Energy is shifted according to the fermi-level, which is marked by the dash line.
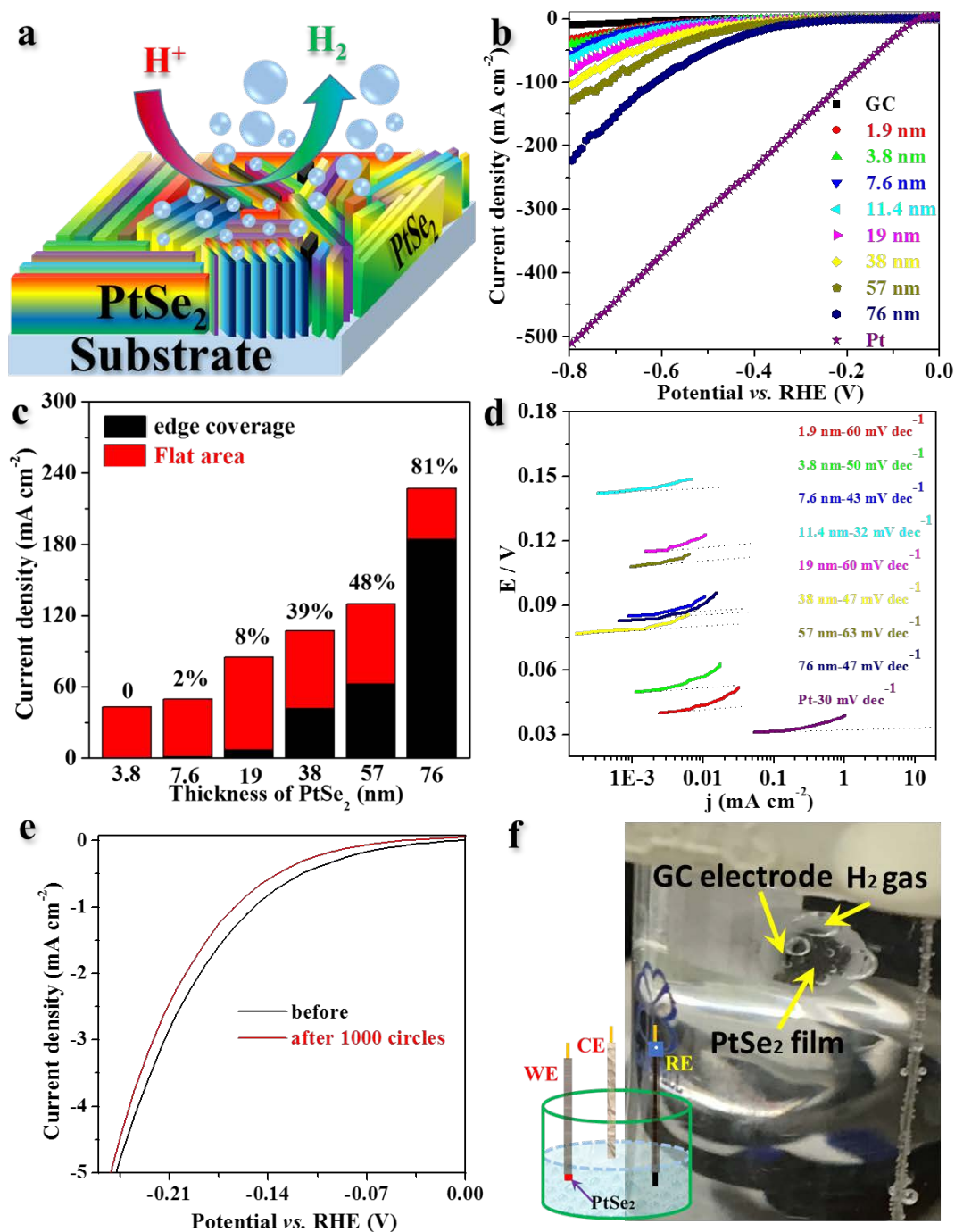
Figure 4. The electrocatalytic performance of PtSe$_2$ film. (a) Schematic illustration of the HER activity of PtSe$_2$ film; (b) Polarization curves; (c) The relationship between the current density and edge sites density on the top surface of PtSe$_2$ film; (d) Tafel plots corresponding to (b); (e) Polarization curves of PtSe$_2$ film: before and after 1000 circles. (f) Digital photos show the H$_2$ bubbles on PtSe$_2$/GC electrode. The inset shows the working electrode (WE), counter electrode (CE) and reference electrode (RE) in the measurement system.

Table 1. The relationship between the thickness of $PtSe_2$ film and the corresponding edge site density

Thickness	3.8 nm	7.6 nm	19 nm	38 nm	57 nm	76 nm
Edge density	~0	~2%±0.2%	~8%±0.3%	~39%±1%	~48%±2%	~81%±5%

Table 2. Comparison of TOFs of the edge-terminated $PtSe_2$, MoS_2 and $MoSe_2$ Films.

Materials	exchange current density (A/cm^2)	exchange current per site (A/site)	TOF （S^{-1}）	Reference
MoS_2	2.2×10^{-6}	4.1×10^{-21}	0.013	34
$MoSe_2$	2.0×10^{-6}	4.5×10^{-21}	0.014	34
$PtSe_2$ （76nm）	1.5×10^{-5}	1.7×10^{-20}	0.054	This work